Engineering the Berreman mode in mid-infrared polar materials

Irfan Khan,[1] Zhaoyuan Fang,[1] Milan Palei,[1] Junchi Lu,[1] Leland Nordin,[2] Evan L. Simmons,[3] Owen Dominguez,[1] S. M. Islam,[4] Huili Grace Xing,[4,5] Debdeep Jena,[4,5] Viktor A. Podolskiy,[3] Daniel Wasserman,[2] and Anthony J. Hoffman[1,*]

[1]*Department of Electrical Engineering, University of Notre Dame, Notre Dame, IN 46556, USA*
[2]*Department of Electrical and Computer Engineering, University of Texas Austin, Austin, TX 78758, USA*
[3]*Department of Physics and Applied Physics, University of Massachusetts Lowell, Lowell, Massachusetts 01854, USA*
[4]*Department of Materials Science and Engineering, Cornell University, Ithaca, NY 17853, USA*
[5]*School of Electrical and Computer Engineering, Cornell University, Ithaca, NY 14853, USA*
*ajhoffman@nd.edu

Abstract: We demonstrate coupling to and control over the broadening and dispersion of a mid-infrared leaky mode, known as the Berreman mode, in samples with different dielectric environments. We fabricate subwavelength films of AlN, a mid-infrared epsilon-near-zero material that supports the Berreman mode, on materials with a weakly negative permittivity, strongly negative permittivity, and positive permittivity. Additionally, we incorporate ultra-thin AlN layers into a GaN/AlN heterostructure, engineering the dielectric environment above and below the AlN. In each of the samples, coupling to the Berreman mode is observed in angle-dependent reflection measurements at wavelengths near the longitudinal optical phonon energy. The measured dispersion of the Berreman mode agrees well with numerical modes. Differences in the dispersion and broadening for the different materials is quantified, including a 13 cm^{-1} red-shift in the energy of the Berreman mode for the heterostructure sample.

1. Introduction

In recent years, long-wavelength nanophotonics has attracted considerable attention. The growing interest in the mid-infrared and far-infrared portions of the electromagnetic spectrum, cumulatively 3–60 μm, is due in large part to the potential for advancing applications in spectroscopy and sensing [1–6], optical free-space and on-chip communications [7,8], and radiative cooling [9,10]. Much of the recent progress has leveraged surface phonon polaritons (SPhPs) to increase light-matter interactions [4,11–14]. These hybrid excitations couple electromagnetic radiation to vibrations of a polar crystal lattice (phonons) and strongly confine light to the surface or interface of polar materials. A SPhP is supported at the interface between materials with optical permittivity values of opposite signs. Polar dielectric materials exhibit a negative permittivity in a spectral region dictated by the optical phonon energies, which reside in the mid-infrared and far-infrared for most dielectric and semiconductor materials [11,12,15].

In the spectral region between the longitudinal optical (LO) and transverse optical (TO) phonon frequencies, a polar dielectric exhibits negative permittivity. This spectral region, known as the *Reststrahlen* band of the material, can be leveraged as a low-loss, negative permittivity frequency band. For polar dielectrics, the loss depends on the scattering time of optical phonons, whereas the loss is governed by electron scattering in metals. The longer scattering times of optical phonons in polar dielectrics compared to electrons in metals and doped semiconductors result in epsilon-near-zero and negative permittivity materials with lower loss [11,12]. These reduced

losses make SPhPs an excellent long-wavelength alternative for applications where SPPs are limited by the loss of the metal or doped semiconductor.

In addition to the potential for supporting SPhPs, polar dielectrics are also promising low-loss, epsilon-near-zero (ENZ) materials. At the LO phonon energy, the real part of the permittivity vanishes, and the imaginary part can be similarly small [11–13,16]. Epsilon-near-zero materials have been used for engineering the frequency response of optical antennas [17–19], wavefront engineering [20,21], and controlling emissivity [22,23]. Furthermore, sub-wavelength layers of ENZ material support a leaky propagating mode known as the Berreman mode [24]. Ultra-thin layers of polar dielectrics ($t < \lambda/100$, where t is the polar dielectric thickness and λ is the Berreman mode wavelength) on a metal ground plane have been used to demonstrate near-perfect absorption of mid-infrared light and selective thermal emission with an emissivity that approaches unity [15]. For these ultra-thin materials, the dispersion of the mode depends weakly on the tangential component of the wavevector, $k_{||}$. Thicker sub-wavelength materials ($t \approx \lambda/10$) also exhibit strong absorption and selective emission, but the dispersion is stronger, with the Berreman mode blue-shifting with increasing $k_{||}$, and the coupling is weaker [15,24]. Recently, hybrid excitations that couple SPPs to the Berreman mode have been demonstrated as a mechanism for engineering the dispersion of ENZ modes, which are limited in applications due to the small group velocity and limited propagation length [25] . Controlling coupling to the Berreman mode and the dispersion of the mode via the surrounding dielectric environment is an alternate approach to engineering the Berreman mode and could open new opportunities for leveraging ENZ material for new applications in nanophotonics.

Here, we demonstrate control over the dispersion of the Berreman mode excited on subwavelength films of AlN by depositing or growing the sub-wavelength films ($t \approx \lambda/10$) on materials with disparate optical permittivity functions. We also show how the Berreman mode can be shifted energetically by amounts exceeding the broadening of the mode via strain in ultra-thin layers of AlN and GaN. The samples are characterized using angle- and wavelength-dependent reflection spectroscopy and simulated using a transfer matrix method. We map the dispersion of the Berreman mode for 1.2 μm thick AlN on Mo, SiC, and GaN and interleaved layers of AlN and GaN on a SiC substrate. We show how coupling to the Berreman mode is also influenced by the material under the AlN films and by incorporating the AlN into the AlN/GaN heterostructure. We demonstrate a spectral red-shift of approximately 10 cm^{-1} for modes excited in the AlN/GaN heterostructure compared to modes excited on bulk AlN.

2. Methods

The samples we study all have a top film thickness of 1.2 μm, with one sample having an AlN/GaN heterostructure thickness of 1.2 μm. These subwavelength films are thin enough to support the Berreman mode and thick enough to exhibit dispersion in the Berreman mode energy with increasing incident angle. The four samples we characterize are summarized in Fig. 1(a). Sample I consists of 1.2 μm of AlN grown via molecular beam epitaxy (MBE) on a SiC substrate. Sample II consists of a Si carrier substrate, 100 nm Mo ground plane, and 1.2 μm of polycrystalline AlN deposited via sputtering. Sample III consists of 1.2 μm of AlN on 2 μm of GaN grown using MBE on a SiC substrate. Finally, sample IV consists of 12 pairs of 50/50 nm thick AlN/GaN layers grown via MBE, a total heterostructure thickness of 1.2 μm, on a SiC substrate. Samples I to III allow us to demonstrate control over the characteristics of the Berreman mode through the material below the ENZ AlN film. We show how the permittivity of the substrate affects coupling and confinement of the mode. We use sample IV to demonstrate the effects of surrounding the ENZ AlN film with positive permittivity material.

We model the optical permittivity of each material using an analytic model for the bulk material. The frequency-dependent complex dielectric permittivity for the AlN, GaN, and SiC layers are
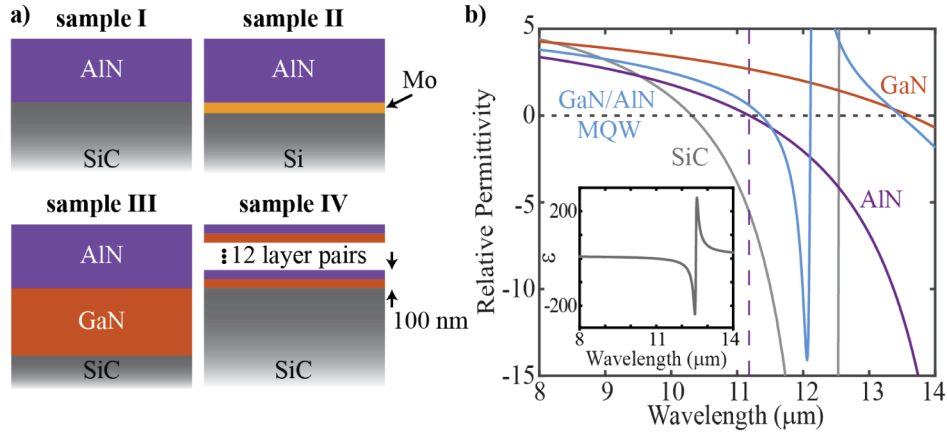
Fig. 1. (a) Summary of the samples characterized in this work. The bulk AlN layers are 1.2 μm thick for samples I, II, and III. The Mo layer is 100 nm thick for sample II and the GaN layer is 2 μm thick. (b) Relative permittivity versus wavelength for GaN (red), AlN (purple), and SiC (gray). The blue line shows the effective permittivity in the growth direction for sample IV. The inset shows the relative permittivity of SiC over a larger range.

modeled using an isotropic permittivity with a single oscillator:

$$\epsilon_m(\omega) = \epsilon_{\infty,m}\left(1 + \frac{\omega_{LO,m}^2 - \omega_{TO,m}^2}{\omega_{TO,m}^2 - \omega^2 - i\omega\gamma_m}\right)$$

where $m = [\text{AlN, GaN, SiC}]$ indicates the selected material; $\epsilon_{\infty,m}$ is the high-frequency permittivity; $\omega_{LO,m}$ and $\omega_{TO,m}$ are the frequencies of the LO and TO phonon, respectively; and γ_m is the scattering rate. We use isotropic models because the materials are polycrystalline, the anisotropy is relatively small (compared to broadening), and isotropic models have been used successfully previously for similar materials [12,17,20,26–29]. Table 1 summarizes the parameters that were used for each material. These material parameters were taken from literature and adjusted less than 5% to improve agreement between the experimental data and numerical models. To determine the scattering rate, we fit the width of the reflection dip associated with the TO phonon. The scattering rate, which is related to the optical quality of the film, differs for the AlN films realized via MBE and sputtering, 9 and 12.5 cm^{-1}, respectively. For the AlN/GaN heterostructure, we red shift the AlN phonon frequencies and blue shift the GaN phonon frequencies. We attribute this shift to strain in the heterostructure due to a lattice mismatch in the AlN and GaN layers; this shift agrees well with existing models of optical phonon energies in strained III-nitride layers [30,31].

The wavelength-dependent permittivity of Mo is modeled using Drude model

$$\epsilon_{Mo}(\omega) = \epsilon_{\infty,Mo} - \left(\frac{\omega_{p,Mo}^2}{\omega^2 + i\gamma_{Mo}\omega}\right)$$

where $\epsilon_{\infty,Mo} = 1$ is the static permittivity for Mo; $\omega_{p,Mo} = 60,200$ cm^{-1} is the plasma frequency; and $\gamma_{Mo} = 412$ cm^{-1} is the scattering rate [32].

Figure 1(b) shows the calculated permittivity near the AlN LO phonon energy for each of the materials, excluding Mo because it is strongly negative in this spectral region. The vertical dashed line at 11.18 μm (894.45 cm^{-1}) indicates where the real part of the permittivity for AlN is zero, $Re(\epsilon_{AlN}) = 0$. For appropriately thin films, a Berreman mode, which couples to free-space

Table 1. Material Optical Constants[a],[b],[c]

Material	ε_∞	ω_{TO} (cm^{-1})	ω_{LO} (cm^{-1})	γ (cm^{-1})
AlN (MBE)[a]	4.6	656.8	889.8	9
AlN (sputtered)	4.6	656.8	890.0	12.5
AlN (strained)[b]	4.6	649.5	880.3	9
GaN[c]	5.35	530	735	3.5
GaN (strained)[b]	5.35	537.7	742.4	3.5
SiC[c]	6.56	797	970	5

[a]From Appl. Phys. Lett. 111, 091105 (2017).
[b]From Phys. Rev. B 68, 165335 (2003).
[c]From Appl. Phys. Lett. 107, 081108 (2015).

light, can be excited at and around this wavelength. The real part of the permittivity for GaN is positive at this wavelength, while the real parts of the permittivity for SiC and Mo are both negative at this wavelength, $\epsilon_{0,Mo}(\lambda = 11.18\,\mu m) = -3736 + 1721i$. Therefore, samples I, II, and III can be used to show how a weakly negative, strongly negative, and positive permittivity material under an ENZ material influence the Berreman mode. Sample IV demonstrates how interleaving the ENZ material with a positive permittivity material affects the characteristics of the AlN Berreman mode.

Polarization-dependent reflection spectra are collected using a Bruker Vertex v80 vacuum spectrometer with a Pike VeeMAX III for incident light from 30 to 75 deg. with a step size of 5 deg. The transverse magnetic (TM) or transverse electric (TE) polarization of the incident light, see Fig. 2(a), is selected using a KRS-5 wire grid polarizer prior to the VeeMAX III. A cooled HgCdTe detector and mid-infrared globar source are used for all measurements.
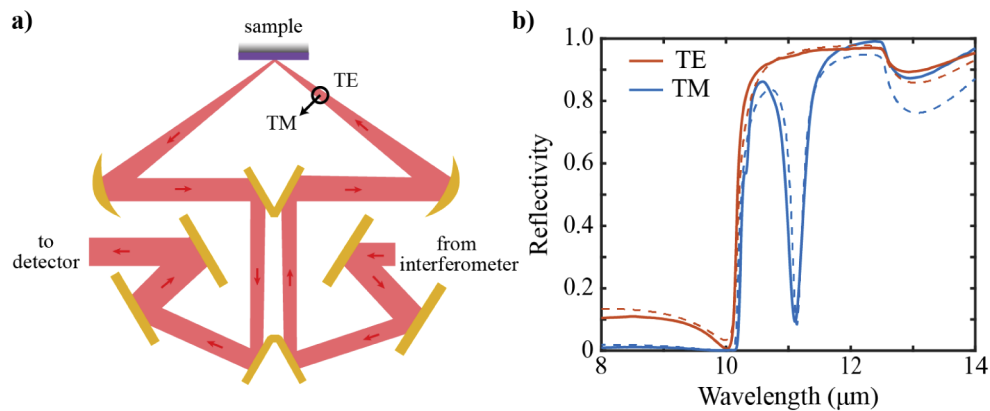

Fig. 2. (a) Schematic of the experimental setup and definition of TM and TE polarizations. Mirrors are represented by gold shapes. (b) Measured (solid) and calculated (dashed) TM and TE reflectivity of sample I for light incident at 45 deg.

Single channel spectra for each of the samples and a gold-coated glass coverslip, which served as a near-perfect reflector, are collected using a resolution of 4 cm^{-1} for all measurements. Angle-dependent reflection spectra for each polarization are obtained by dividing the single channel spectrum of the sample by the single channel spectrum of the gold-coated coverslip reference for each incident angle.

3.   Results and discussion

Figure 2(b) shows the measured TE and TM reflection spectra for sample I when light is incident at 45 deg. The calculated reflection is shown using dashed lines. The TE reflection spectrum approaches unity beyond 10.2 μm. This increase in reflectivity is expected for polar materials at wavelengths near and between the LO and TO phonons. For sample I, the increase in reflectivity at 10.2 μm is due to the SiC substrate, which has LO phonons at 970 cm^{-1} (10.3 μm). At wavelengths where the photon energy is similar in energy to the AlN LO phonon, *c.a.* 11.18 μm, the permittivity of AlN approaches zero, Fig. 1(b). The strong dip in the TM reflection spectrum at 11.1 μm in Fig. 2(b) indicates coupling of free-space light to the Berreman mode in the AlN layer; such a dip is not observed in the TE reflection spectrum.

In Fig. 3 we show the measured TM reflection versus wavelength and incident angle for each of the samples. These images are assembled from many spectra such as those shown in Fig. 2(b) and use a common colorscale for comparison. Each of the samples exhibits a dip in the reflection at energies close to the AlN LO phonon, indicating excitation of the Berreman mode. We overlay the calculated dispersion of the mode for each of the samples, obtained via rigorous coupled-wave analysis (RCWA) based numerical simulations, using white dots. As mentioned earlier, we red-shift (blue-shift) the phonon frequencies of AlN (GaN) to account for tensile (compressive) strain in sample IV [25]. Overall, there is strong agreement between the measured and calculated spectra. We confirm the nature of these Berreman modes—and other modes evidenced by additional dips in the measured reflection spectra—by calculating the field distribution for each of the samples using COMSOL Multiphysics.

Samples I and II each exhibit a single dip in the reflection spectra in Fig. 3. Figure 4 shows $|E_z|^2$ and $|H|^2$ at $\lambda = 11.1$ μm, the wavelength of the dip in the experimental data. For both samples, there is an enhancement of the electric field in the AlN layer. The fields for sample I are weakly confined by the bottom SiC layer, which has a slightly negative permittivity, and leak into air, Fig. 4(a). For sample II, again the fields leak into air, but they are confined more strongly by the 100 nm Mo layer beneath AlN, Fig. 4(b). The enhancement of the field in the ENZ AlN layer and the leaky nature of the mode observed in both samples are characteristic of the Berreman mode [24].

The TM reflection spectrum of sample III exhibits three dips, as seen in Fig. 3. Figure 5 shows the calculated fields for each of these modes at 45 deg. incidence. The first dip at 11.1 μm corresponds to the Berreman mode as confirmed via the field plots for this wavelength in Fig. 5(a). However, two longer-wavelength dips at approximately 12 and 13.5 μm are also identified in the reflection measurements of Fig. 3(c). These spectral dips are reproduced in the numerical models and correspond to a leaky metal-insulator-metal propagating waveguide mode (12 μm) and a GaN Berreman mode (13.5 μm). The leaky metal-insulator-metal waveguide mode, Fig. 5(b), consists of a sinusoidal mode in the positive-permittivity GaN layer and decaying fields in the SiC and AlN layers, which exhibit a negative permittivity at $\lambda = 12$ μm, Fig. 1(b). The stronger confinement provided by the SiC layer compared to the AlN layer is due to the more negative permittivity of SiC at this wavelength. The Berreman mode in the GaN layer is similar to that in the AlN layers in that an enhanced electric field is observed in the GaN layer, Fig. 5(c). The electric field decays relatively slowly in the AlN layer on top of the GaN layer due to the slightly negative permittivity. As with the AlN Berremamn mode, the GaN Berreman mode leaks into a propagating mode in free-space.

Two dips are identified in the reflection measurements for sample IV, Fig. 3. The first at $\lambda = 11.3$ μm corresponds to a Berreman mode enabled by the vanishing permittivity of the AlN layers. The field plots at this wavelength, shown in Fig. 5(d), exhibit enhancement of the electric field in the ENZ AlN layers. Similarly, the dip at $\lambda = 13.4$ μm is due to the excitation of a Berreman mode in the GaN layers. At this longer wavelength, the electric field is enhanced in the GaN layers, Fig. 5(e). The spectral locations of both modes agree well with our simulations
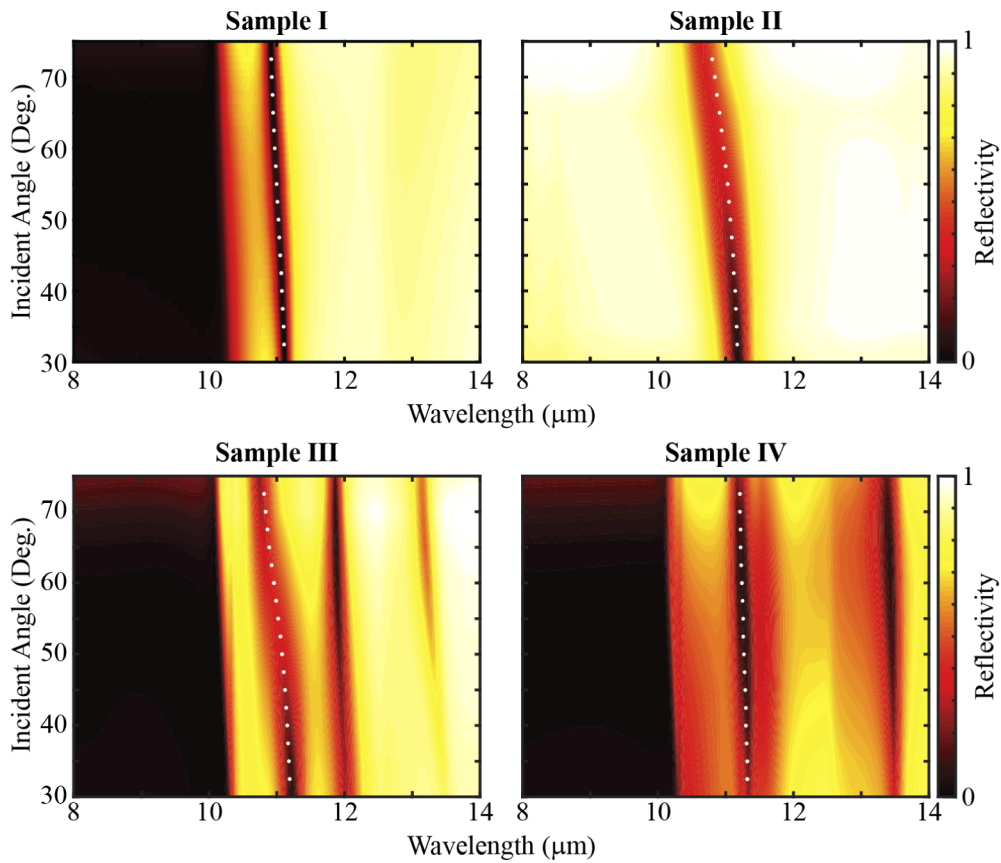
Fig. 3. Measured reflectivity of each sample versus wavelength and incident angle for TM polarized light. The white dots indicate the minimum in the calculated reflection spectrum using RCWA code.
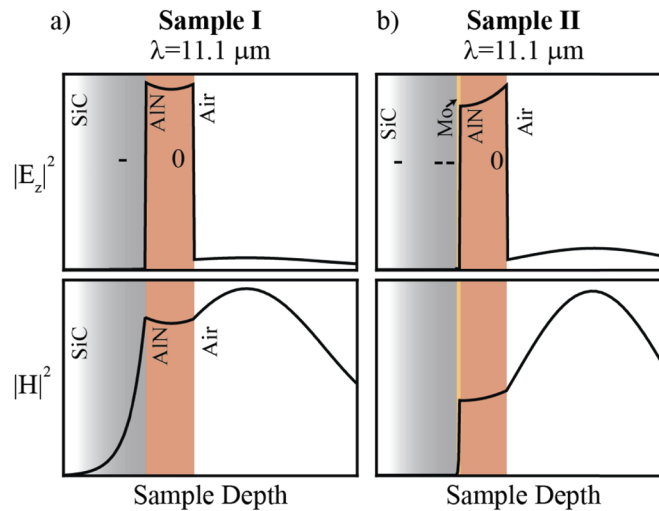

Fig. 4. Calculated field versus sample depth at $\lambda = 11.1\,\mu m$ for incident angle of 45° for samples (a) I and (b) II. The sign of the real part of the permittivity for each material is indicated "0" or "-". A "- -" indicates that the optical permittivity of Mo is strongly negative.
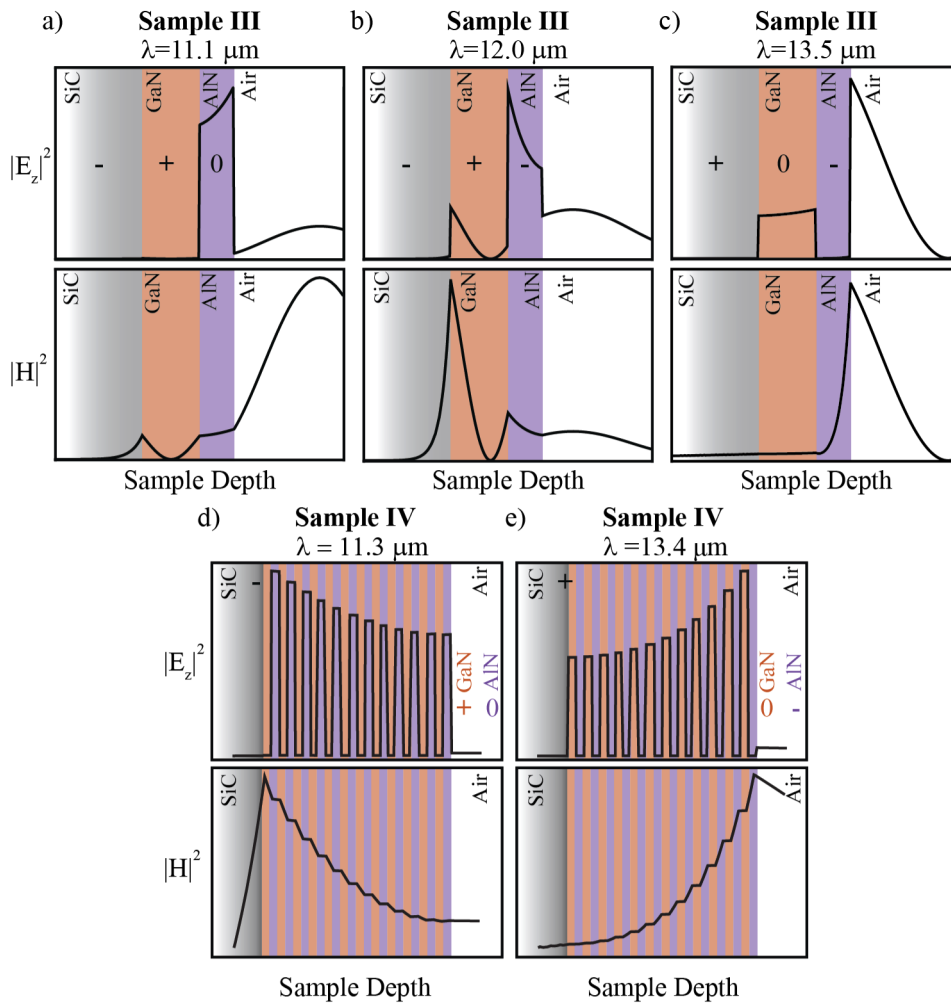
Fig. 5. Calculated field versus sample depth for (a) – (c) sample III and (d) - (e) sample IV at several wavelengths. The sign of the real part of the optical permittivity for a given material is indicated in the top panel of each sample using "0", "-", or "+".

after red-shifting the LO phonon energy, Fig. 3. Note that the collective modes in Sample IV can be described in terms of either bulk plasmon [33] or effective medium theory [34] terminology. In the latter case, the excitation of the Berreman mode occurs in the vicinity of the ENZ condition of the effective permittivity (in the growth direction) of the multilayer stack, $\epsilon_{eff} = (d_{GaN} + d_{AlN})/\left(\frac{d_{GaN}}{\epsilon_{GaN}} + \frac{d_{AlN}}{\epsilon_{AlN}}\right)$, with d_m being thickness of the material m. The effective permittivity is shown in Fig. 1(b).

While each of the samples exhibits a Berreman mode around the AlN ENZ spectral region, the characteristics of that mode vary significantly by sample. The dispersion of the Berreman mode versus $k_{||}$, the tangential component of the incident wavevector, for each of the samples is shown in Fig. 6(a). The dashed lines are guides for the eye. The strongest dispersion is observed for sample II, which blue-shifts by more than 40 cm^{-1} over the range of measured angles. Sample IV exhibits the weakest dispersion, blue-shifting less than 7 cm^{-1}. Figure 6(b) depicts the evolution of the spectral width of the mode, measured as the full-width at half minimum, for each of the samples. Sample II exhibits the broadest mode for each $k_{||}$. The peak broadening of Sample II, 0.32 μm, is more than two times the peak broadening of samples I and IV, 0.11 and 0.01 μm, respectively.
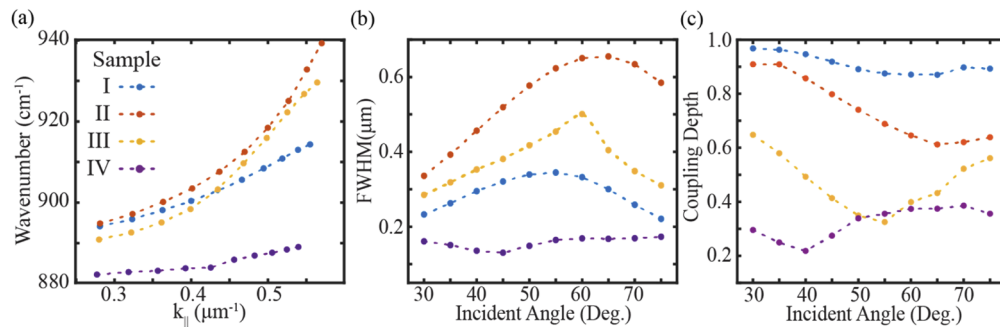

Fig. 6. (a) Measured dispersion of the AlN Berreman mode. (b) Broadening versus incident angle measured as the full width at half minimum of the reflectivity dip. (c) Depth of the reflectivity dip due to coupling to the Berreman mode.

Finally, Fig. 6(c) depicts a measure of the coupling between the Berreman mode and free-space light. This coupling parameter is determined by fitting the reflection spectrum in the spectral neighborhood of the Berreman mode using a Gaussian lineshape with a linear slope baseline and reporting the difference between the fit minimum and the value of the linear baseline at the wavelength of the fit minimum. The dip in the reflection approaches unity for sample I, indicating strong coupling of the Berreman mode to the incident light. The coupling is much weaker for the multi-layered sample IV, which can be as low as 0.2. Thus, while the broadening is smaller for the Berreman mode excited in sample IV, coupling to the mode is smaller and the dispersion is flatter, presenting a trade-off for devices that leverage this mode.

4. Conclusions

We demonstrate coupling of free-space light to the Berreman mode in sub-wavelength AlN thin films on different dielectric and metal layers using angle-dependent reflection measurements. In all, we characterize four samples, where the dielectric environment around the AlN ENZ layer is controlled via material selection. Each sample exhibits a strong dip in the TM reflection indicating coupling to the Berreman mode. The field distribution for this mode, and modes corresponding to additional dips in the reflectivity spectra, are calculated using finite element methods. The dispersion of the Berreman mode is measured and agrees well with RCWA models.

Finally, we analyze the spectral broadening and coupling to the modes for each of the samples, demonstrating the ability to engineer many aspects of the optical characteristics of the Berreman mode through material selection, including a spectral shift of 13 cm^{-1} that arises from strain in the AlN layers due to the lattice mismatch between AlN and GaN. The work presented here offers an approach to integrating the Berreman mode into optical devices aimed at narrow-band emission in the mid-infrared. New devices enabled by engineering the dispersion, coupling, and broadening of the Berreman mode may be possible.

Funding

Disclosures

The authors declare no conflicts of interest.

References

1. J. A. Dieringer, A. D. McFarland, N. C. Shah, D. A. Stuart, A. V. Whitney, C. R. Yonzon, M. A. Young, X. Y. Zhang, and R. P. Van Duyne, "Surface enhanced Raman spectroscopy: new materials, concepts, characterization tools, and applications," Faraday Discuss. **132**, 9–26 (2006).
2. S. Lal, S. Link, and N. J. Halas, "Nano-optics from sensing to waveguiding," Nat. Photonics **1**(11), 641–648 (2007).
3. E. Di Fabrizio, S. Schlucker, J. Wenger, R. Regmi, H. Rigneault, G. Calafiore, M. West, S. Cabrini, M. Fleischer, N. F. van Hulst, M. F. Garcia-Parajo, A. Pucci, D. Cojoc, C. A. E. Hauser, and M. Ni, "Roadmap on biosensing and photonics with advanced nano-optical methods," J. Opt. **18**(6), 063003 (2016).
4. M. Autore, P. N. Li, I. Dolado, F. J. Alfaro-Mozaz, R. Esteban, A. Atxabal, F. Casanova, L. E. Hueso, P. Alonso-Gonzalez, J. Aizpurua, A. Y. Nikitin, S. Velez, and R. Hillenbrand, "Boron nitride nanoresonators for phonon-enhanced molecular vibrational spectroscopy at the strong coupling limit," Light: Sci. Appl. **7**(4), 17172 (2018).
5. E. Shkondin, T. Repan, M. E. A. Panah, A. V. Lavrinenko, and O. Takayama, "(High Aspect Ratio Plasmonic Nanotrench Structures with Large Active Surface Area for Label-Free Mid-Infrared Molecular Absorption Sensing)," ACS Appl. Nano Mater. **1**(3), 1212–1218 (2018).
6. T. G. Folland, G. Y. Lu, A. Bruncz, J. R. Nolen, M. Tadjer, and J. D. Caldwell, "Vibrational Coupling to Epsilon-Near-Zero Waveguide Modes," ACS Photonics **7**(3), 614–621 (2020).
7. S. Kruk, F. Ferreira, N. Mac Suibhne, C. Tsekrekos, I. Kravchenko, A. Ellis, D. Neshev, S. Turitsyn, and Y. Kivshar, "Transparent Dielectric Metasurfaces for Spatial Mode Multiplexing," Laser Photonics Rev. **12**(8), 1800031 (2018).
8. F. C. B. Maia, B. T. O'Callahan, A. R. Cadore, I. D. Barcelos, L. C. Campos, K. Watanabe, T. Taniguchi, C. Deneke, A. Belyanin, M. B. Raschke, and R. O. Freitas, "Anisotropic Flow Control and Gate Modulation of Hybrid Phonon-Polaritons," Nano Lett. **19**(2), 708–715 (2019).
9. M. M. Hossain and M. Gu, "Radiative Cooling: Principles, Progress, and Potentials," Adv. Sci. **3**(7), 1500360 (2016).
10. Y. Zhai, Y. G. Ma, S. N. David, D. L. Zhao, R. N. Lou, G. Tan, R. G. Yang, and X. B. Yin, "Scalable-manufactured randomized glass-polymer hybrid metamaterial for daytime radiative cooling," Science **355**(6329), 1062–1066 (2017).
11. J. D. Caldwell, L. Lindsay, V. Giannini, I. Vurgaftman, T. L. Reinecke, S. A. Maier, and O. J. Glembocki, "Low-loss, infrared and terahertz nanophotonics using surface phonon polaritons," Nanophotonics **4**(1), 44–68 (2015).
12. K. Feng, W. Streyer, Y. Zhong, A. J. Hoffman, and D. Wasserman, "Photonic materials, structures and devices for Reststrahlen optics," Opt. Express **23**(24), A1418–A1433 (2015).
13. S. Foteinopoulou, G. C. R. Devarapu, G. S. Subramania, S. Krishna, and D. Wasserman, "Phonon-polaritonics: enabling powerful capabilities for infrared photonics," Nanophotonics **8**(12), 2129–2175 (2019).
14. A. Kumar, T. Low, K. H. Fung, P. Avouris, and N. X. Fang, "Tunable Light-Matter Interaction and the Role of Hyperbolicity in Graphene-hBN System," Nano Lett. **15**(5), 3172–3180 (2015).
15. L. Nordin, O. Dominguez, C. M. Roberts, W. Streyer, K. Feng, Z. Fang, V. A. Podolskiy, A. J. Hoffman, and D. Wasserman, "Mid-infrared epsilon-near-zero modes in ultra-thin phononic films," Appl. Phys. Lett. **111**(9), 091105 (2017).
16. N. C. Passler, C. R. Gubbin, T. G. Folland, I. Razdolski, D. S. Katzer, D. F. Storm, M. Wolf, S. De Liberato, J. D. Caldwell, and A. Paarmann, "Strong Coupling of Epsilon-Near-Zero Phonon Polaritons in Polar Dielectric Heterostructures," Nano Lett. **18**(7), 4285–4292 (2018).
17. O. Dominguez, L. Nordin, J. C. Lu, K. J. Feng, D. Wasserman, and A. J. Hoffman, "Monochromatic Multimode Antennas on Epsilon-Near-Zero Materials," Adv. Opt. Mater. **7**(10), 1800826 (2019).
18. J. Kim, A. Dutta, G. V. Naik, A. J. Giles, F. J. Bezares, C. T. Ellis, J. G. Tischler, A. M. Mahmoud, H. Caglayan, O. J. Glembocki, A. V. Kildishev, J. D. Caldwell, A. Boltasseva, and N. Engheta, "Role of epsilon-near-zero substrates in the optical response of plasmonic antennas," Optica **3**(3), 339–346 (2016).

19. S. A. Schulz, A. A. Tahir, M. Z. Alam, J. Upham, I. De Leon, and R. W. Boyd, "Optical response of dipole antennas on an epsilon-near-zero substrate," Phys. Rev. A **93**(6), 063846 (2016).

20. A. Alu, M. G. Silveirinha, A. Salandrino, and N. Engheta, "Epsilon-near-zero metamaterials and electromagnetic sources: Tailoring the radiation phase pattern," Phys. Rev. B **75**(15), 155410 (2007).

21. G. Briere, B. Cluzel, and O. Demichel, "Improving the transmittance of an epsilon-near-zero-based wavefront shaper," Opt. Lett. **41**(19), 4542–4545 (2016).

22. S. Molesky, C. J. Dewalt, and Z. Jacob, "High temperature epsilon-near-zero and epsilon-near-pole metamaterial emitters for thermophotovoltaics," Opt. Express **21**(S1), A96–A110 (2013).

23. I. Liberal and N. Engheta, "Manipulating thermal emission with spatially static fluctuating fields in arbitrarily shaped epsilon-near-zero bodies," Proc. Natl. Acad. Sci. U. S. A. **115**(12), 2878–2883 (2018).

24. S. Vassant, J. P. Hugonin, F. Marquier, and J. J. Greffet, "Berreman mode and epsilon near zero mode," Opt. Express **20**(21), 23971–23977 (2012).

25. E. L. Runnerstrom, K. P. Kelley, T. G. Folland, J. R. Nolen, N. Engheta, J. D. Caldwell, and J. P. Maria, "Polaritonic Hybrid-Epsilon-near-Zero Modes: Beating the Plasmonic Confinement vs Propagation-Length Trade-Off with Doped Cadmium Oxide Bilayers," Nano Lett. **19**(2), 948–957 (2019).

26. K. J. Feng, W. Streyer, S. M. Islam, J. Verma, D. Jena, D. Wasserman, and A. J. Hoffman, "Localized surface phonon polariton resonances in polar gallium nitride," Appl. Phys. Lett. **107**(8), 081108 (2015).

27. W. Streyer, K. Feng, Y. Zhong, A. J. Hoffman, and D. Wasserman, "Selective absorbers and thermal emitters for far-infrared wavelengths," Appl. Phys. Lett. **107**(8), 081105 (2015).

28. W. Streyer, S. Law, A. Rosenberg, C. Roberts, V. A. Podolskiy, A. J. Hoffman, and D. Wasserman, "Engineering absorption and blackbody radiation in the far-infrared with surface phonon polaritons on gallium phosphide," Appl. Phys. Lett. **104**(13), 131105 (2014).

29. W. Streyer, K. Feng, Y. Zhong, A. J. Hoffman, and D. Wasserman, "Engineering the Reststrahlen band with hybrid plasmon/phonon excitations," MRS Commun. **6**(1), 1–8 (2016).

30. J. M. Wagner and F. Bechstedt, "Properties of strained wurtzite GaN and AlN: Ab initio studies," Phys. Rev. B **66**(11), 115202 (2002).

31. N. C. Passler, I. Razdolski, D. S. Katzer, D. F. Storm, J. D. Caldwell, M. Wolf, and A. Paarmann, "Second Harmonic Generation from Phononic Epsilon-Near-Zero Berreman Modes in Ultrathin Polar Crystal Films," ACS Photonics **6**(6), 1365–1371 (2019).

32. M. A. Ordal, R. J. Bell, R. W. Alexander, L. L. Long, and M. R. Querry, "Optical properties of fourteen metals in the infrared and far infrared: Al, Co, Cu, Au, Fe, Pb, Mo, Ni, Pd, Pt, Ag, Ti, V, and W," Appl. Opt. **24**(24), 4493–4499 (1985).

33. I. Avrutsky, I. Salakhutdinov, J. Elser, and V. Podolskiy, "Highly confined optical modes in nanoscale metal-dielectric multilayers," Phys. Rev. B **75**(24), 241402 (2007).

34. A. J. Hoffman, L. Alekseyev, S. S. Howard, K. J. Franz, D. Wasserman, V. A. Podolskiy, E. E. Narimanov, D. L. Sivco, and C. Gmachl, "Negative refraction in semiconductor metamaterials," Nat. Mater. **6**(12), 946–950 (2007).